Gu *et al. Biochar* (2026) 8:133
https://doi.org/10.1007/s42773-026-00651-7

Biochar

ORIGINAL RESEARCH Open Access

pH-regulated surface chemistry of nano-biochar for selective silver ion reduction: the pivotal role of superoxide radicals

Shiguo Gu[1], Dandan Wang[1], Tongtong Wang[2] and Wei Zhu[1*]

Abstract

Silver ion (Ag^+) pollution in aquatic systems poses serious ecological and health threats, demanding effective and controllable remediation technologies. This study investigates the pH-dependent reduction of Ag^+ by nano-biochar (nano-BC) synthesized via ball milling from wood chip-derived bulk biochar pyrolyzed at 400 °C (nano400) and 700 °C (nano700). Using advanced characterization techniques and free radical detection, we found that the reduction of Ag^+ to silver nanoparticles (AgNPs) by nano-BC is strongly pH-dependent: no AgNPs are formed under acidic-neutral conditions (pH 6.5–7.5), while weakly alkaline environments (pH 8.5–9.5) promote efficient reduction with the highest yield at pH 9.5. AgNPs formation follows pseudo-first-order kinetics, and nano400 exhibits a reaction rate constant approximately 2.5 times higher than that of nano700, showing significantly faster reduction kinetics. Nano400 outperforms nano700, attributed to its abundant oxygen-containing functional groups (e.g., phenolic hydroxyl groups, 3.01 mmol g^{-1}), which enhanced its electron-donating capacity. Mechanistic studies reveal that superoxide radicals ($O_2^{\cdot-}$) act as the key intermediates, generated via the synergistic effect of deprotonated functional groups and persistent free radicals (PFRs) in nano-BC under alkaline conditions. Excessive nano-BC dosage (> 10 mg L^{-1} for nano400, > 20 mg L^{-1} for nano700) inhibits AgNPs formation, likely via reduced interfacial reactive sites and reactive oxygen species (ROS) self-consumption. This study clarifies the core mechanism of pH-regulated Ag^+ reduction by nano-BC, providing theoretical support for nano-BC remediation of Ag^+-contaminated water.

Highlights

- Nano400 outperforms nano700 for rich oxygen groups
- Nano-BC mediates pH-controlled Ag^+ reduction, with effective AgNPs synthesis only at pH 8.5–9.5.
- Nano400 exhibits 2.5-fold faster AgNPs formation kinetics than nano700 at pH 9.5.
- Alkaline-induced $O_2^{\cdot-}$ from nano-BC's deprotonated groups and PFRs mediates Ag^+ reduction.

Keywords Nano-biochar, Silver ion reduction, pH regulation, Superoxide radical

*Correspondence:
Wei Zhu
wzhu@issas.ac.cn
Full list of author information is available at the end of the article

Springer

Graphical Abstract

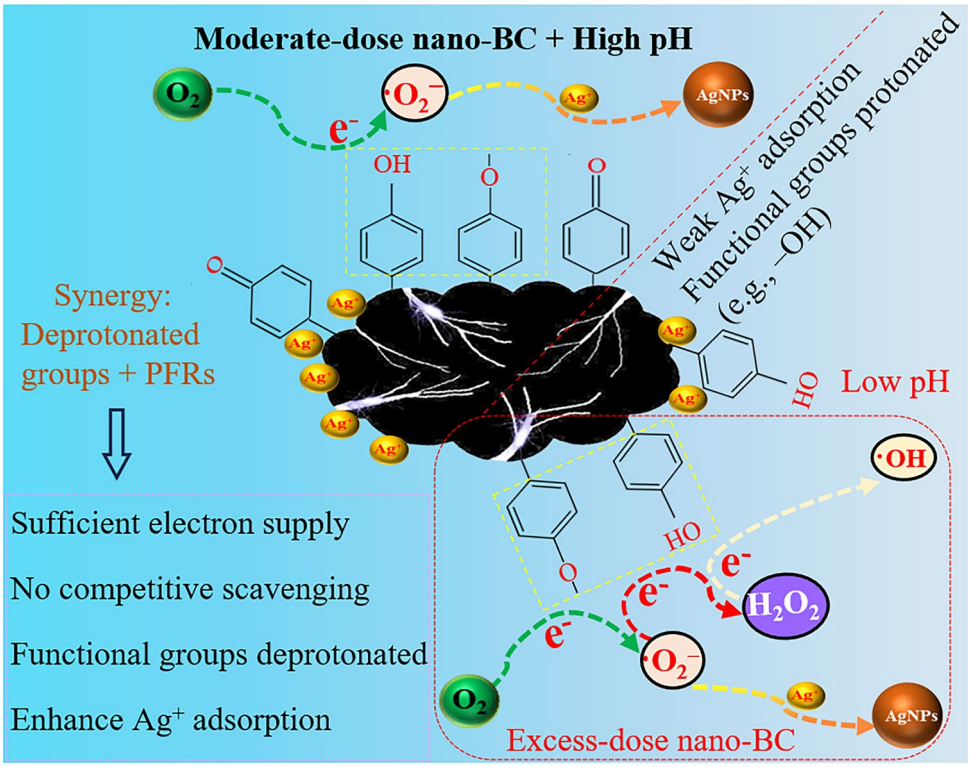

1 Introduction

Silver ions (Ag^+) are extensively used in industrial applications due to their antimicrobial activity, excellent electrical conductivity, and ductility, but they pose significant environmental risks due to their toxicity and high mobility in ecosystems (Liu et al. 2023; Nguyen et al. 2024). Thus, the recovery of silver from wastewater is crucial not only for mitigating its ecological toxicity but also for reclaiming this valuable metal resource (Shao et al. 2023). The natural water environment is estimated to contain Ag^+ concentrations ranging from approximately 1 to 1000 ng L^{-1} (Cymes et al. 2017), with treated effluents reaching up to 5 mg L^{-1} (Zhao et al. 2021; Ge et al. 2022). As reported by Vrček et al., silver nanoparticles (AgNPs) have a markedly reduced toxicity to human hepatoblastoma cells compared with Ag^+, with concentrations for induced toxicity at 50% cell loss values being 50 mg L^{-1} and 0.5 mg L^{-1} for AgNPs and Ag^+, respectively (Vrček et al. 2016). Previous studies have shown that the uptake rate constants of Ag^+ in plants are 67–87 times higher than those of AgNPs (Dang et al. 2020). These findings underscore the critical importance of transforming Ag^+ into less toxic forms, such as AgNPs, to minimize their adverse effects on ecosystems and human health.

Biochar, a pyrogenic carbon-rich material, is widely used in soil amendment, as it can significantly improve soil fertility and provide multiple soil benefits (Wang et al. 2023; Mekonnen et al. 2025). In general, the pyrolysis-induced physical degradation of bulk biochar (bulk-BC, 0.04–20 mm) results in a biochar nanoparticle (nano-BC, < 100 nm) yield ranging from 0.47% to 2.36% (Wang et al. 2013; Gao et al. 2014; Liu et al. 2018). To date, researchers have produced nano-BC from bulk-BC via eco-friendly and energy-efficient nanotechnology methods (e.g., ball milling, microwave pyrolysis, and thermo-flash exfoliation) (Lian and Xing 2024; Sun et al. 2025). Among several preparation techniques, ball milling can process bulk-BC into fine nano-BC. Nano-BCs have a lower negative zeta potential, 19.2–31.8% more oxygen, and more persistent free radicals (PFRs) than bulk-BC (Liu et al. 2018), making these stable and highly active particles crucial in transforming states of metals (Ruan et al. 2019; Rashid et al. 2022; Zhu et al. 2023; Gu et al. 2025). It has been reported that 6% of nano-BC adheres to the

root surfaces of rice plants, thus forming an important root-BC interface that directly affects the oxidation of ferrous ions (Gu et al. 2022). Similarly, aeration with O_2 in biochar–ascorbic acid systems enhanced the formation of superoxide radicals ($O_2^{\cdot-}$) via electron transfer with biochar PFRs, boosting bisphenol A removal rates up to 69.4% (Zhu et al. 2024). Moreover, the presence of highly PFRs on the surface of nano-BC provides an additional layer of reactivity that can be used to passivate heavy metals. Simulated sunlight drives the formation of $O_2^{\cdot-}$ from dissolved oxygen via nano-BC, facilitating the photoreduction of Hg(II) to Hg(0) (Li et al. 2020). Additionally, biochar has been reported to assist the reduction of Cr(VI) to Cr(III) and act as an electron shuttle, facilitating the transfer of electrons from soil-relevant organic acids (Xu et al. 2019). Although nano-BC-derived free radicals show strong metal reduction potential as demonstrated above, the exact role of free radicals in Ag^+ reduction is poorly investigated in green reduction systems (Hanna et al. 2022; Kaliappan et al. 2025). Thus, we hypothesized that free radicals on nano-BC surfaces would mediate interfacial reduction reactions, thereby altering the valence and morphology of Ag^+.

The pH level plays a pivotal role in the route of reduction reactions involving carbonaceous material-bound reductive moieties and reduction-sensitive pollutants such as Ag^+ (Cao et al. 2019; Huang et al. 2019). For example, soil organic matter reduced Ag^+ to AgNPs only under neutral and alkaline conditions (7.0 − 8.6) (Huang et al. 2019). Besides, Ag^+ was reported to activate phenolic hydroxyl groups on oxidized graphene to provide electrons for the reduction of Ag^+ under alkaline conditions (≥ 7.4) (Cao et al. 2019). Furthermore, these results emphasize that the pH of the environment can be manipulated to enhance the formation of AgNPs. Importantly, biochar oxidation mechanisms vary with pH, with acidic and neutral conditions favoring As(III) oxidation via hydroxyl radicals (·OH) and H_2O_2 from phenolic −OH, while alkaline conditions promote oxidation by quinoid C = O (Zhong et al. 2019). In addition, biochar inherently has a negatively charged surface and alkaline properties, which endow it with a strong Ag^+ adsorption capacity and further facilitate the interfacial redox reactions between biochar and Ag^+ (Tomczyk et al. 2020; Peng et al. 2021). Collectively, pH level is a critical factor influencing both the reduction of Ag^+ to AgNPs and the reduction mechanisms of biochar, as it determines the availability of reactive species and the pathways of these reactions. Consequently, manipulating the pH of the environment can serve as an effective strategy to enhance AgNPs formation and optimize the biochar-mediated reduction processes.

Existing biochar-metal reduction and nanoparticle synthesis studies lack systematic pH-dependent mechanism clarification and definitive identification of key radical intermediates, as well as quantitative nano-BC structure–activity correlations and dosage inhibition insights. Therefore, the major objectives of this study were to: (1) examine the ability of nano-BC for Ag^+ reduction under different pH conditions; (2) investigate the impact of various reduction active components on reduction of Ag^+ by nano-BC; (3) clarify the mechanism of reduction of Ag^+ under various pH conditions. In this study, various techniques were employed, including high-resolution transmission electron microscopy (HRTEM), Fourier transform infrared spectroscopy (FTIR), X-ray photoelectron spectrometer (XPS), Boehm titration analysis method, and electron paramagnetic resonance (EPR), to characterize the surface and structural properties of nano-BC. This research may provide potentially significant insights into how nano-BC affects the reduction of Ag^+ to AgNPs across a broad range of pH values.

2 Materials and methods

2.1 Materials and chemicals

Silver nitrate ($AgNO_3$) with a purity grade of 99.8% was obtained from Sigma-Aldrich. All the other reagents of analytical grade or superior were acquired from Solarbio Science & Technology Co., Ltd., situated in Beijing, China. The pH of aqueous solution was adjusted using NaOH and HCl, with concentrations ranging from 0.1 to 1 M. Ultrapure water (> 18.2 MΩ cm^{-1}) was used for all experiments.

2.2 Preparation and characterization of nano-BC

Bulk-BC was produced from wood chips crushed and sieved through a 2.0 mm sieve by slow pyrolysis in a tubular reactor. The reactor was heated at a rate of 10 °C min^{-1} from room temperature to 400 or 700 °C and held for 120 min under N_2 atmosphere. These two temperatures represent typical low- and high-temperature pyrolysis, which can well distinguish the differences in surface functional groups, persistent free radicals, and electron-donating capacity of nano-BC (Lian et al. 2020). To obtain nano-BC, 1.0 g of bulk-BC was mixed into a 150 mL agate jar filled with 100 g agate balls with diameters 6 mm, 3 mm, and 1 mm, respectively, ensuring a constant mass ratio of 1:100 between the biochar and the balls. The agate jars containing the mixture were milled in a TJX-410 planetary ball mill (Tianjin Dongfang Tianjin Technology Co., Ltd.) at 300 rpm min^{-1} for 12 h to produce BC particles with a size of < 100 nm. The resulting

nano-sized biochar, obtained from the bulk-BC processed at 400 °C and 700 °C, was labeled as nano400 and nano700, respectively. The morphology and nanoscale dimensions of nano-BC were analyzed using an HRTEM (JEOL JEM-2100F, Japan) operating voltage at 200 kV. FTIR spectroscopy analysis was performed on biochar samples using a Thermo Scientific Nicolet iS5 instrument, operating in the range from 400 to 4000 cm^{-1}. XPS (Thermo Scientific K-Alpha, USA) was utilized to conduct an analysis of the surface chemical compositions of biochar. The C 1 s hydrocarbon peak at 284.8 eV served as the reference for calibrating binding energies, and the XPSPEAK software was employed for deconvolving the C 1 s spectra. A modified Boehm titration analysis was employed to characterize the phenolic –OH, carboxyl, and lactonic groups of biochar, with the detailed methodology presented in Text S1 (Uchimiya et al. 2010). 20 mg of solid nano-BC was analyzed for the PFRs in a quartz tube using a German-manufactured EPR (Bruker A300) spectrometer at 25 ℃. The instrument settings were as follows: 1.92 mW microwave power, 9.85 GHz microwave frequency, and 1.00 G modulation amplitude. With the receiver gain at 1.00×10^3, the analysis included a scan width of 200 G, a time constant of 10.24 ms, a conversion time of 30.00 ms, and a scan time of 30.72 s. The intensity of spin signals was determined via calibration against the 2,2-diphenyl-1-picrylhydrazyl (DPPH) standard. A CHI610E workstation coupled with a three-electrode cell was utilized to perform room-temperature electrochemical measurements for assessing the mediated electrochemical reduction and oxidation properties of nano-BCs (Text S2). Dynamic light scattering (ZEN3600, Malvern, UK) with a scattering angle of 173° was applied to monitor the intensity-weighted hydrodynamic diameter and aggregation kinetics of nano-BC suspensions at varied pH values. All measurements were conducted at 25 °C over a 15 min period with 15 s sampling intervals, and suspension pH was tuned to 6.5, 7.5, 8.5, 9.0, 9.5, and 10 using 0.1 or 1 M HCl and/or NaOH solutions.

2.3 Ag^+ reduction and characterization of the formed AgNPs

All batch experiments were conducted in a 50 mL brown glass (light-protected) containing 0.5 mM $AgNO_3$ solution, and the reaction was incubated for 10 min. Nano-BC was dispersed into 50 mL of 0.5 mM Ag^+ solution to achieve final concentrations of 5, 10, 20, 40, or 60 mg L^{-1}. During the reaction, the desired pH value (i.e., 6.5, 7.5, 8.5, 9.0, 9.5, or 10 ± 0.1) of the aqueous solution was adjusted by 0.1 or 1 M HCl and/or NaOH solutions. The formation of AgNPs suspensions was tracked by UV–visible spectroscopy (UV-1800, Shimadzu, Japan) at 300–600 nm. The obtained AgNPs were characterized using HRTEM to analyze their crystal structure and chemical composition coupled with selected area electron diffraction (SAED). The relative abundance of the AgNPs was assessed through the implementation of Energy Dispersive Spectroscopy (EDS) analysis. Total silver concentrations in aqueous solutions were quantified via inductively coupled plasma mass spectrometry (ICP-MS, ICAP-TQ, Thermo) combined with the cloud point extraction method. Briefly, 50 mL aliquots of the reaction samples were subjected to drying followed by microwave-assisted digestion at 190 °C for 30 min (CEM Corp., Matthews, NC), with a 3 mL 1:1 (v/v) HNO_3/ultrapure water mixture as the digestant. The digested solution was subjected to 0.22 μm filtration, subsequently diluted to 50 mL with Milli-Q ultrapure water, and then analyzed by ICP-MS. The method for the determination of AgNPs by single-particle ICP-MS (SP-ICP-MS) has been established in our previous work (Gu et al. 2025), with detailed procedures provided in Text S3. Reaction solution of the aqueous system was collected at 0, 1, 3, 5, 7, 9, 11, and 13 min, with the synthesis of AgNPs monitored via SP-ICP-MS. A parallel control check (CK) experiment without nano-BC was performed under identical conditions to evaluate the spontaneous reduction of Ag^+ in the absence of biochar. Pseudo-first-order kinetics were used to characterize the reduction process (Adegboyega et al. 2012) with calculations performed according to Eq. 1.

$$-\ln(C_0/C_t) = kt \tag{1}$$

where C_0 and C_t are the concentrations of AgNPs at time beginning and time t, respectively; k is the pseudo-first-order rate constant.

To exclude direct electron transfer from deprotonated phenolic hydroxyl groups, anoxic control experiments were performed in sealed brown vials. The reaction solution was purged with high-purity N_2 for 30 min to completely remove dissolved oxygen prior to the reaction. All other parameters were consistent with those under oxic conditions (0.5 mM Ag^+, 10 mg L^{-1} nano-BC, pH 9.5, 10 min reaction in the dark). After incubation, AgNPs formation was monitored by UV–Vis spectroscopy over 300–600 nm.

2.4 Free radical determination

The generation of free radicals in the nano-BC-containing Ag^+ reduction system was investigated using probe molecules and colorimetric reagents (Fu et al. 2018; Zhang et al. 2020). During the reduction of Ag^+, the probe molecules 2,3-bis(2-methoxy-4-nitro-5-sulfophenyl)-2H-tetrazolium-5-carboxanilide (XTT), terephthalic acid (TPA), and furfuryl alcohol (FFA) were chosen to quantify the generation of $O_2^{\cdot-}$, ·OH, and $^1O_2$, respectively. Briefly, an initial concentration of 0.05 mM

XTT, 1.00 mM TPA, and 0.45 mM FFA was added into each of the reaction mixtures. The concentrations of XTT formazan, TPA residue, and FFA loss were monitored, according to the methodology presented in Text S4. To verify the crucial role of $O_2^{\cdot-}$ in Ag^+ reduction, a quenching assay was carried out using superoxide dismutase (SOD, 150 U mL^{-1}) as an $O_2^{\cdot-}$ scavenger in the reduction system consisting of 0.5 mM Ag^+ and 10 mg L^{-1} nano-BC at pH 9.5. Furthermore, EPR spectroscopy (Bruker A300, Germany) was applied at room temperature to directly identify the generated $O_2^{\cdot-}$ using dimethyl-pyrroline N-oxide (DMPO) as the spin-trapping agent. After reacting for 10 min, an aliquot of the suspension was sampled and mixed with freshly prepared DMPO solution in methyl alcohol to stabilize and trap $O_2^{\cdot-}$ radicals. The mixed solution was immediately subjected to EPR detection, with further experimental details provided in Text S5.

The concentrations of H_2O_2 in biochar systems were measured according to the colorimetry method (Zhang et al. 2020). 1 mL of 0.5 M sulfuric acid solution was added into a centrifuge tube (15 mL) containing 1 mL of the reaction solution, and then 0.1 mL of 15 wt% titanyl sulfate was added. The mixture solution was adjusted to a final volume of 10 mL using ultrapure water. The H_2O_2 concentration was quantified at a wavelength of 410 nm using a UV–vis spectrophotometer. Then, the absorbance was recorded at 410 nm using water as a blank.

2.5 Statistical analysis

The experiments were each repeated in triplicate, and the data are reported as mean values ± standard deviations. Statistical significance of differences between treatments ($p < 0.05$) was assessed using one-way ANOVA, coupled with the Duncan test. The statistical analyses of all data were carried out with the assistance of IBM SPSS Statistics version 26.0 (USA). Error bars in all figures represent the standard deviation of triplicate parallel samples to reflect experimental random errors and data reproducibility.

3 Results and discussion

3.1 Nano-BC characterization

The surface morphology of nano-BC examined by HRTEM revealed that both nano-BCs were present as irregular, near-elliptical nanostructures with particle sizes below 100 nm (Fig. S1). Figure 1A shows the C 1 s XPS spectra with three distinct peaks appearing at 284.6 eV (C=C/C–C), 285.2 eV (C–OH), and 286.7 eV (C=O), corresponding to the reported literature (Dong et al. 2013; Lian et al. 2018). The nano700 exhibits a higher content of C=C/C–C bonds (43.45%) than nano400 (20.15%), suggesting a richer presence of sp^2- and sp^3-hybridized carbons as well as graphene-like structures within nano700 due to higher heat treatment temperatures. Conversely, nano400 possesses a greater proportion of oxygen-containing functionalities, specifically –OH groups (60.95%) and C=O groups (18.90%). The chemically reactive functional groups on the nano-BC surface were also identified via FTIR (Fig. 1B), including –OH at 3440 cm^{-1}, $-CH_2$ at 2920, –COOC at 1700, aromatic C=C at 1600 cm^{-1}, aliphatic–OH at 1440 cm^{-1}, C–O at 1090 cm^{-1}, and aromatic CH at 877 cm^{-1}. Meanwhile, the oxygen content of nano400 calculated from Boehm analysis is higher than that of nano700, especially with phenolic hydroxyl groups as high as 3.01 mmol g^{-1} (Bardestani and Kaliaguine 2018). These results indicate that nano400 contains a higher abundance of oxygen-functional groups than nano700. These XPS and FTIR spectral differences directly determine the electron supply capacity and subsequent $O_2^{\cdot-}$ yield for Ag^+ reduction. Nano700 has higher carbon content (70.72%) and ash (12.65%) but lower oxygen (12.02%) and nitrogen (2.06%) compared to nano400 (Table S1), consistent with its higher pyrolysis temperature leading to carbonization and loss of volatile functional groups. The lower O/C and (O+N)/C ratios of nano700 (Tables S1 and S2) correlate with its higher sp^2 carbon content (XPS C 1 s spectrum) and fewer oxygen groups (FTIR), supporting its graphene-like structure. Meanwhile, nano400's higher polarity (Tables S1 and S2) aligns with its abundant –OH and C=O groups (XPS/FTIR) and Boehm titration results (phenolic OH = 3.01 mmol g^{-1}). The ζ potential values of nano400 consistently exhibited higher absolute magnitudes compared to nano700 across the tested pH range (2–10), directly correlating with its greater abundance of oxygen-containing functional groups (Fig. 1D). Notably, under weakly alkaline conditions (around pH 9.5), the increased deprotonation of these oxygen-containing functional groups may further enhance the negative surface charge, thereby strengthening the electrostatic adsorption of cationic Ag^+ onto the nano-BC surface. The data collectively validate nano400's superior aqueous compatibility for applications requiring stable dispersion (e.g., environmental remediation), while nano700's lower surface charge favors non-polar matrices. Specifically, pyrolysis temperature reshapes the surface chemistry and carbon skeleton of nano-BC, creating clear disparities between nano400 and nano700. Low-temperature pyrolysis (400 °C) avoids severe thermal decomposition of oxygenated functional groups, leaving 3.01 mmol g^{-1} phenolic hydroxyl groups and abundant edge defects to stabilize high levels of PFRs; high-temperature treatment at 700 °C, however, triggers massive deoxygenation and the formation of compact sp^2 carbon structures, limiting electron transfer and $O_2^{\cdot-}$ generation. The 1.56-fold

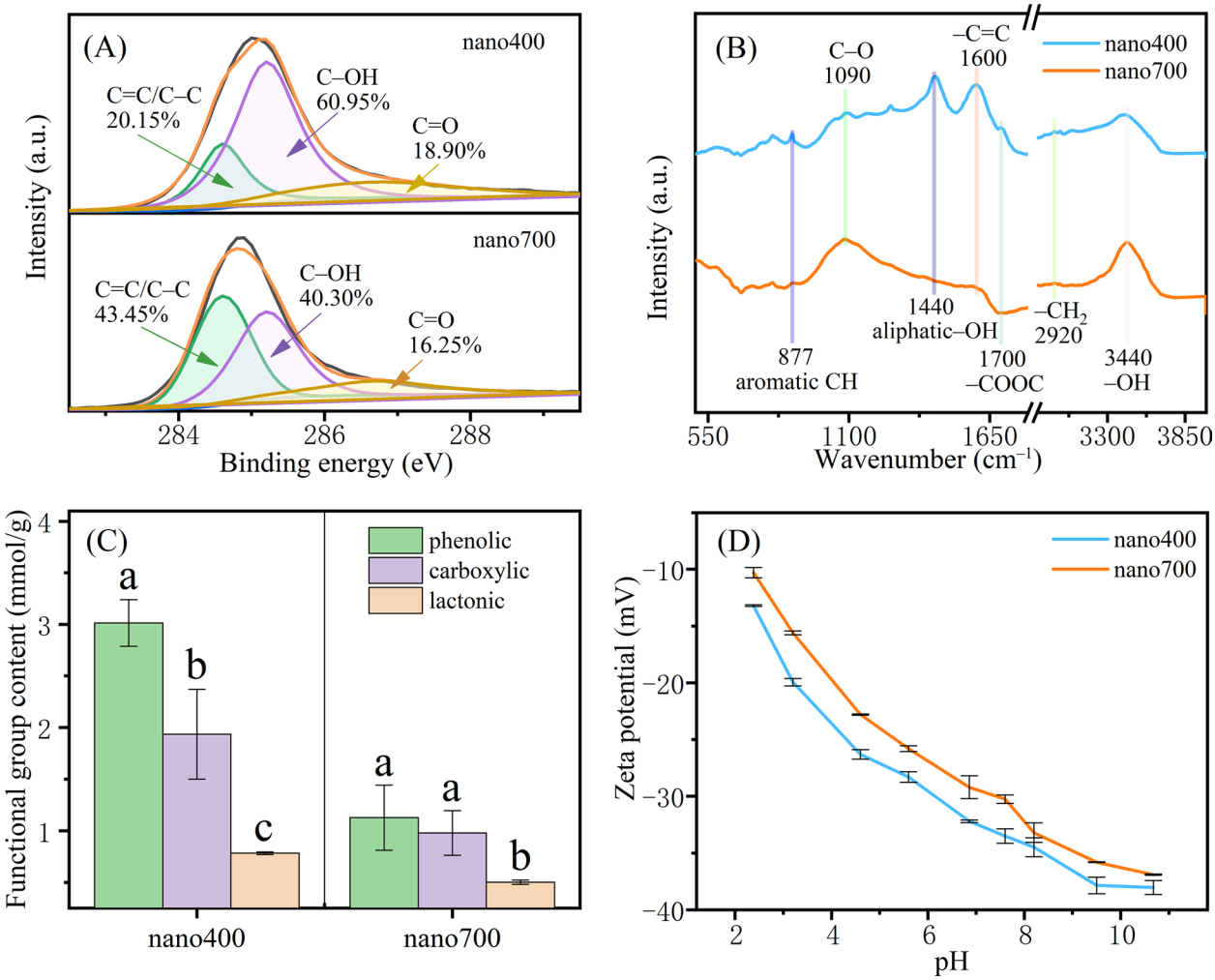

Fig. 1 Characterization of nano-BC (nano400 and nano700). **A** high-resolution C 1 s XPS spectra; **B** FTIR spectra; **C** functional group content; and **D** ζ potentials in different solution pHs. Error bars represent the standard deviation of the mean of the triplicates

higher electron-donating capacity of nano400 enhances directly its reactivity toward heavy metal ions (e.g., Ag^+), a discrepancy fully controlled by temperature-driven changes in surface functional groups and persistent free radical content.

3.2 pH-dependent synthesis of AgNPs mediated by nano-BC in aqueous solution

The reduction of Ag^+ to AgNPs in aqueous solutions under controlled pH conditions was systematically investigated using UV–Vis spectroscopy. UV–Vis spectroscopy revealed a prominent peak at 410 nm, which is a well-documented indicator of spherical AgNPs formation (Fig. 2) (Hou et al. 2013; Zhang et al. 2016). The UV–Vis absorbance at 410 nm quantifies Ag^+ reduction yield, which is directly linked to $O_2^{\cdot-}$ production enabled via FTIR/XPS-identified phenolic functional groups. As shown in Fig. 2, it was found that no AgNPs were formed in the nano-BC system at acidic to neutral pH (6.5 to 7.5), likely due to the protonation of surface functional groups, accompanied by insufficient reactive sites, and limited electron-donating capacity. It was reported that the surface functional groups of nano-BC are protonated to generate H^+ in a lower pH environment (Mahmoud et al. 2024). This observation is consistent with the inhibited $O_2^{\cdot-}$ generation from phenol-like groups under acidic conditions, which consequently suppresses the reduction of Ag^+ to AgNPs (Huang et al. 2019). However, as the pH increased to weakly alkaline levels (pH 8.5–9.5), the reduction efficiency improved markedly, with the highest AgNPs yield observed at pH 9.5. Consistently, the colloidal aggregation of nano-BCs was regulated by solution pH, and the maximum colloidal stability was observed at pH 9.5 (Figs. S2 and S3). This enhancement can be attributed to the increased electron-donating ability of functional groups on nano-BC (e.g., phenolic and carboxyl

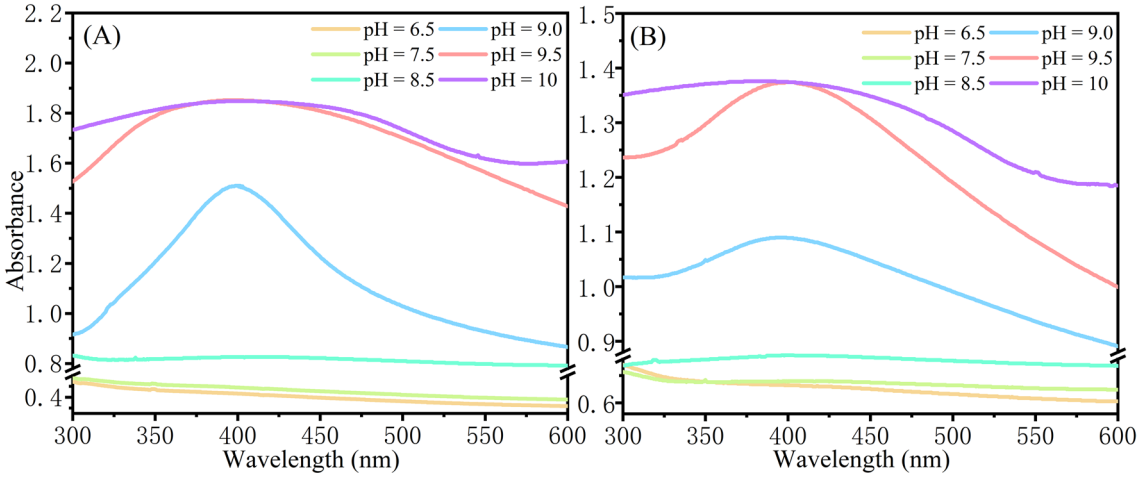

Fig. 2 Effects of pH on the reduction of Ag^+ in the presence of 10 mg L^{-1} nano400 (**A**) and nano700 (**B**)

groups) under alkaline conditions, which facilitates the reduction of Ag^+ to AgNPs (see more discussion below).

Excessive nano-BC dosage (> 10 mg L^{-1} for nano400 or > 20 mg L^{-1} for nano700) correlated with reduced AgNPs formation, likely due to disrupted electron transfer pathways from potential donors to Ag^+ (Fig. S4). Compared to nano700, nano400 exhibits more abundant oxygen-containing groups (–OH, –COOH), which enhance oxygen reduction and thereby nano400 drives higher $O_2^{\cdot-}$ generation, evidenced by elevated XTT formazan levels in Fig. S5. Phenolic groups contributed to $O_2^{\cdot-}$ production in biochar due to their redox-active nature (Lian et al. 2021). We observed that nano400 contained 167.35% more phenolic OH than nano700, consistent with the trend in $O_2^{\cdot-}$ quantum yields. The disproportionation of $O_2^{\cdot-}$ into $^1O_2$ (Fig. S6) and H_2O_2 (Fig. S7) is triggered by electron transfer from excessive nano-BC. Additionally, the loss of TPA indicates that increased biochar content accelerates ·OH production via electron donation to H_2O_2 (Fig. S8). The proposed mechanisms of reactive oxygen species (ROS) formation during the reduction of excess nano-BC from Ag^+ to AgNPs are illustrated in Fig. S9. Specifically, this study elucidates the pH-dependent role of nano-BC in mediating Ag^+ reduction to AgNPs, where alkaline conditions (pH 8.5–9.5) optimize electron donation from deprotonated functional groups (–OH/–COOH). Excessive nano-BC loading (> 10 mg L^{-1}) inversely suppresses AgNPs formation, probably owing to reduced available reactive sites and aggravated ROS depletion. Notably, nano400's superior $O_2^{\cdot-}$ generation capacity, attributed to its richer phenolic content, underscores the interplay between oxygen-containing groups and ROS-driven Ag^+ reduction. These findings advance the mechanistic understanding of nano-BC as a tunable catalyst for metal nanoparticle synthesis, with implications for environmental and catalytic applications.

3.3 AgNPs formation and characterization

The morphological and structural features of AgNPs formed under varying pH conditions were systematically characterized. The increase in AgNPs yield with rising pH, as observed by TEM (Figs. 3A–C), correlates well with the UV–Vis absorption trends at 410 nm. Meanwhile, TEM observations further revealed that nanoparticles formed at optimal pH exhibit a narrow size distribution ranging from 5.88 to 23.53 nm with uniform quasi-spherical morphology. The AgNPs remained well-dispersed during the 10-min reaction, as evidenced by stable UV–Vis absorbance at 410 nm without peak broadening or significant wavelength shift, and TEM images showing predominantly dispersed quasi-spherical nanoparticles (Figs. 3A–C), likely due to electrostatic stabilization from the negatively charged nano-BC surface, though prolonged storage or high ionic strength may induce aggregation. EDS analysis revealed a prominent Ag Lα emission peak at ~ 3 keV (Fig. 3D), confirming the successful formation of metallic AgNPs. Notably, the color transition of colloidal suspensions from pale yellow to deep yellow with increasing pH (7.5–9.5) confirms AgNPs formation, as higher pH enhances Ag^+ reduction (Huang et al. 2019). HRTEM analysis (Fig. 3E) identified distinct lattice fringes with spacings of d = 0.236 nm, d = 0.205 nm, and d = 0.145 nm, corresponding to the {111}, {200}, and {220} crystallographic planes of face-centered cubic Ag (JCPDS No. 04-0783), confirming their metallic nature (Jiang et al. 2016). The SAED patterns (Fig. 3F) further validated the polycrystalline

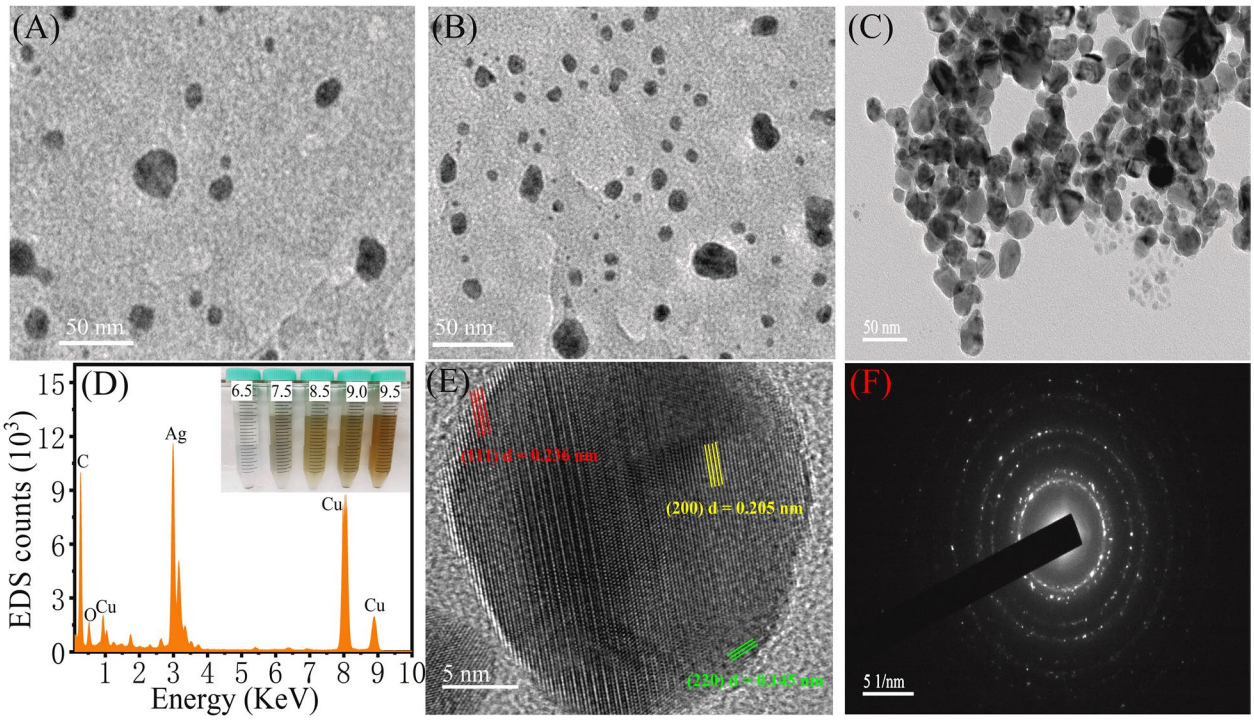

Fig. 3 Identification and characterization of AgNPs generated through nano400-mediated reduction (10 mg L^{-1}) of 0.5 mM Ag^+: **A, B** TEM images of AgNPs at pH 8.5 and 9.0; **C–F** TEM, EDS, HRTEM, and SAED characterization of AgNPs at pH 9.5

structure through diffraction rings indexed to {111}, {200}, and {220} planes (Yang et al. 2017). These findings collectively demonstrate that nano400 acts as an efficient catalyst for Ag^+ reduction under alkaline conditions. The pH-dependent modulation of surface functional group protonation states (e.g., −OH/−COOH) enhances electron transfer kinetics under alkaline conditions, which aligns with the electrochemical mechanisms proposed for biochar-facilitated AgNPs synthesis (Mahmoud et al. 2024). The synergistic role of nano400 in AgNPs formation warrants further investigation into its environmental and catalytic applications.

3.4 Formation kinetics of AgNPs

AgNPs formation kinetics across a gradient of reaction durations were determined by SP-ICP-MS analysis (Fig. 4A), with subsequent kinetic model fitting further applied to resolve the kinetic characteristics of the formation process (Fig. 4B). Kinetic analysis of Ag^+ reduction to AgNPs revealed that rapid, time-dependent nanoparticle formation was exclusive to the experimental system combining nano-BC, $AgNO_3$, and a pH 9.5 environment, while no measurable AgNPs generation was observed in the CK groups throughout the reaction period. The obtained data were well fitted to a pseudo-first-order kinetic model using linear regression ($R^2 > 0.90$) (Adegboyega et al. 2012). The pseudo-first-order kinetic plot showed that the rate constant values for nano400 increase more rapidly over time relative to those for nano700, with nano400 exhibiting a reaction rate constant approximately 2.5 times higher than that of nano700. Previous reports indicate significantly lower Ag^+ reduction rate constants for materials such as particulate organic matter (0.00249 h^{-1}) (Huang et al. 2019) and natural organic matter (0.000175 h^{-1}) (Hou et al. 2013), highlighting the markedly superior catalytic efficiency of nano-BC observed in this study. Additionally, graphene oxide, activated carbon, and carbon nanotubes usually demand UV irradiation or chemical functionalization to realize Ag^+ reduction (Cao et al. 2019; Posachayanan et al. 2024; Zhang et al. 2026), whereas nano-BC enables spontaneous Ag^+ reduction. More importantly, unlike toxic chemical reductants, slow biosynthetic routes, and energy-consuming photocatalytic/electrochemical techniques (Shahzadi et al. 2025; Shapkin et al. 2026), the nano-BC system achieves rapid Ag^+ reduction within ~ 10 min at ambient temperature without external stimulus. Such significant kinetic difference is essentially attributed to the distinct surface and structural properties of the two nano-BCs. Nano400 possesses a far higher abundance of oxygen-containing functional groups such as phenolic hydroxyl groups up

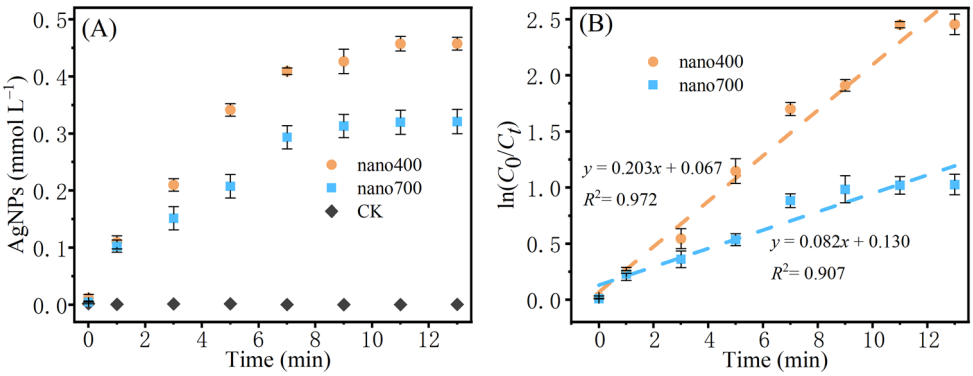

Fig. 4 SP-ICP-MS analysis of AgNPs formed from Ag^+ reduction mediated by nano-BC (10 mg L^{-1}) under different conditions. **A** Concentrations of the newly formed AgNPs in different treatments as a function of time; **B** Dynamic fitting curve of Ag^+ reduction. Error bars represent the standard deviation of the mean of the triplicates

to 3.01 mmol g^{-1} and a higher absolute ζ potential value across the tested pH range than nano700, which endows nano400 with more reactive sites and a more efficient electron transfer rate in the interfacial redox reaction. Meanwhile, electron-donating/accepting capacity quantified from cyclic voltammetry measurements (Fig. S10) confirmed that nano400 has an intrinsic electron-donating capacity approximately 1.56 times that of nano700, which directly contributes to its faster kinetic performance during AgNPs formation. Quantitative structure–activity analysis reveals that nano400, with 2.66-fold higher phenolic –OH content (3.01 vs. 1.13 mmol g^{-1}) than nano700, exhibits a 2.50-fold higher AgNPs formation rate constant. This consistent proportionality provides robust quantitative evidence that phenolic hydroxyl groups serve as the dominant electron-donating structural determinants governing the Ag^+ reduction kinetics of nano-BC.

3.5 Intrinsic mechanism of AgNPs formation

The generation of $O_2^{\cdot-}$ during AgNPs formation in nano-BC suspensions under highly alkaline conditions was investigated using UV–Vis spectroscopy, XTT assays, and EPR analysis (Fig. 5). The UV–Vis spectra (Fig. 5A) exhibit a relatively high characteristic peak at 410 nm, confirming successful AgNPs formation through the reduction of 0.5 mM Ag^+ with 10 mg L^{-1} nano-BC at pH 9.5. At pH 9.5, the deprotonation of oxygen-containing groups may enhance the electron-donating capacity of nano-BC, possibly promote direct interfacial electron transfer to Ag^+, and act synergistically with the generation of $O_2^{\cdot-}$ to jointly drive the reduction of Ag^+. Anoxic (N_2-saturated) control experiments revealed no AgNPs under oxygen-free conditions, indicating negligible direct electron transfer from deprotonated phenolic hydroxyl groups to Ag^+ (Fig. S11). The observed SOD-mediated quenching of $O_2^{\cdot-}$ radicals confirms generation of these reactive species as key intermediates during nano-BC-facilitated reduction of Ag^+ to AgNPs. The reduction in absorbance upon SOD addition confirms that $O_2^{\cdot-}$ radicals are indeed produced and can be quenched, thereby inhibiting the further formation of AgNPs (Fig. S12). This finding aligns with the suggested role of aquatic-derived particulate organic matter in promoting AgNPs formation under highly alkaline conditions (Huang et al. 2019). Simultaneously, it was reported that illumination promoted the formation of $O_2^{\cdot-}$ from dissolved oxygen, which subsequently facilitated the reduction of Ag^+ (Jones et al. 2011). Surface PFRs act as the primary electron donors for $O_2^{\cdot-}$ generation on nano-BC. Formed by homolytic cleavage of phenolic –OH during pyrolysis, PFRs are stabilized via sp^2 carbon conjugation and turbostratic matrix confinement, and their long lifetime and reducing capacity sustain continuous interfacial O_2 activation to yield $O_2^{\cdot-}$ (Zhu et al. 2024; Chen et al. 2025). Notably, the reduction potential of biochar (−0.36 to −0.49 V vs. Ag/AgCl) (Klupfel et al. 2014; Xin et al. 2019) is sufficiently low to enable PFRs to mediate the reduction of O_2 to $O_2^{\cdot-}$ (−0.28 V) (Sun et al. 2019). For example, electron donation from PFRs in biochar to molecular oxygen has been demonstrated to generate $O_2^{\cdot-}$ in aqueous biochar suspensions (Gao et al. 2022; Zhu et al. 2024). As a result, as an effective electron mediator, nano-BC facilitated the interfacial electron transfer to Ag^+, leading to kinetically accelerated AgNPs formation.

Further investigation into the key role of $O_2^{\cdot-}$ in AgNPs formation was conducted using quenching experiments combined with EPR analysis. As the pH value increases, the concentrations of XTT formazan (via $O_2^{\cdot-}$ reduction) produced by nano-BCs exhibit an upward trend (Fig. 5B), which is highly consistent with the formation

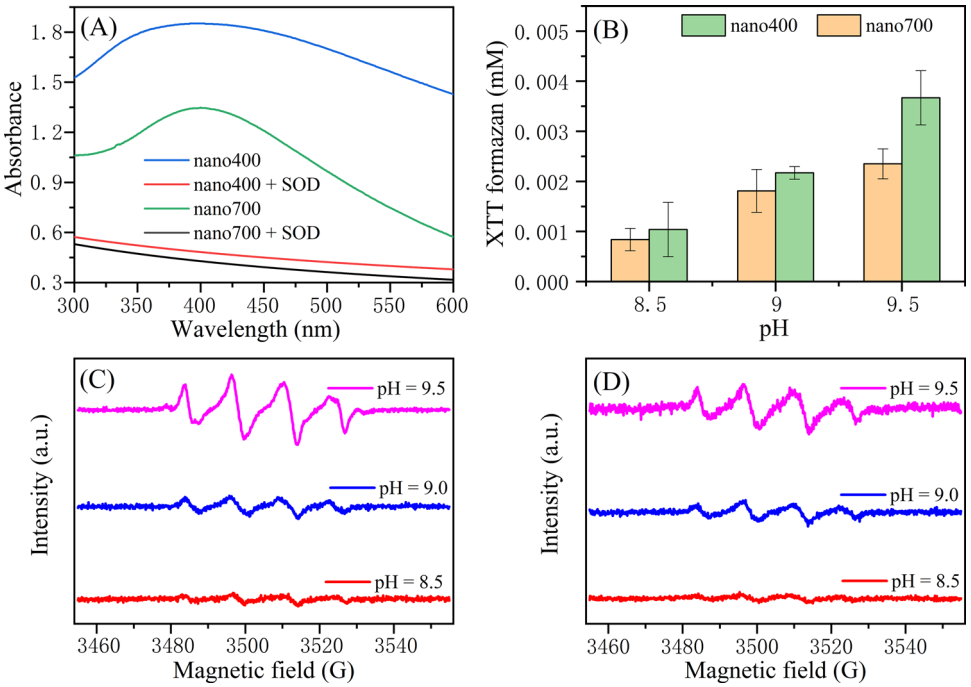

Fig. 5 Production of $O_2^{\cdot-}$ in nano-BC suspension. **A** UV–Vis spectra of AgNPs suspension after 10 min incubation with 20 mg L^{-1} SOD, produced by the reduction of 0.5 mM Ag^+ with 10 mg L^{-1} nano-BC at pH 9.5. **B** XTT formazan and EPR spectra (nano400 (**C**)/nano700 (**D**)) were analyzed at varying pH after 10 min incubation in 0.5 mM Ag^+ with 10 mg L^{-1} nano-BC suspension. Error bars represent the standard deviation of the mean of the triplicates

of AgNPs. Notably, at pH 9.5, nano400 exhibits 1.56-fold higher XTT formazan production compared to nano700 ($p < 0.05$), demonstrating both the pH sensitivity of $O_2^{\cdot-}$ generation and the superior activity of nano400 in superoxide production. Additionally, the characteristic peaks of DMPO-$O_2^{\cdot-}$ spin adducts (Zollo et al. 2025) were detected in nano-BC suspensions across the pH range of 8.5–9.5 (Figs. 5C, D). This pH-dependent enhancement in EPR signal intensity corroborates the earlier observations of increased XTT formazan production at higher pH. It was also found that nano400 generates significantly higher levels of $O_2^{\cdot-}$ than nano700, as evidenced by EPR signals and XTT formazan yields. Consistently, nano400 exhibited 1.4 times higher EPR intensity than nano700 (Fig. S13), which was probably attributed to the higher content of oxygen-containing groups (i.e., –OH, C=O). Electrochemical measurements further confirmed this enhanced redox activity, with nano400 exhibiting an inherent electron-donating capacity approximately 1.56 times higher than nano700 during Ag^+ reduction. This superior $O_2^{\cdot-}$ production capacity directly underpins nano400's enhanced redox activity and faster Ag^+ reduction kinetics. This divergence fundamentally originates from pyrolysis temperature-induced differences in surface functional groups and persistent free radical density, which jointly determine the overall $O_2^{\cdot-}$ generation efficiency and Ag^+ reduction performance. DMPO-$O_2^{\cdot-}$ signals disappeared under anoxic and SOD-quenched conditions, verifying that $O_2^{\cdot-}$ was generated from the reaction between dissolved O_2 and nano-BC surface PFRs. This Ag^+ reduction follows a catalytic pathway rather than a fully stoichiometric reaction: phenolic groups donate initial electrons, while dissolved O_2 continuously regenerates $O_2^{\cdot-}$ to sustain cyclic reduction without net consumption of nano-BC active sites. Collectively, based on all experimental evidence, we propose a coupled interfacial pathway where Ag^+ adsorption on deprotonated nano-BC surfaces (maximized at pH 9.5) acts as an essential prerequisite to immobilize Ag^+, and the interfacial $O_2^{\cdot-}$ produced by PFRs subsequently reduces these surface-bound Ag^+ into AgNPs (Fig. 6). Acidic pH and anoxic control tests further verify that Ag^+ adsorption is indispensable, while $O_2^{\cdot-}$ serves as the exclusive key reductive intermediate for this surface-coupled reaction.

4 Conclusions

This study systematically investigates the pH-dependent reduction of Ag^+ to AgNPs by nano-BC and clarifies the underlying mechanisms, with two types of nano-BC (nano400 and nano700) synthesized via ball milling from wood chip-derived bulk biochar pyrolyzed at 400 °C and

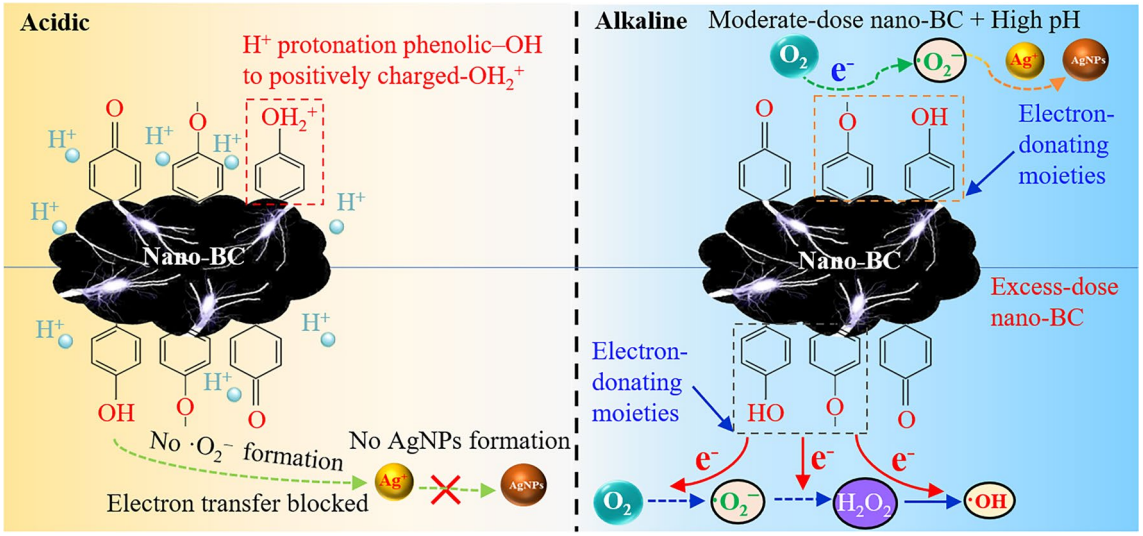

Fig. 6 Schematic illustration of possible mechanisms for pH and dosage co-regulated Ag^+ reduction by nano-BC

700 °C, respectively. The results demonstrate that pH is a decisive factor regulating the reduction process: no AgNPs are formed under acidic to neutral conditions (pH 6.5 − 7.5) due to the protonation of surface functional groups on nano-BC, which generates H^+ that competes with Ag^+ for adsorption sites and inhibits the production of $O_2^{\cdot-}$, while weakly alkaline environments (pH 8.5–9.5) significantly promote Ag^+ reduction with the highest yield at pH 9.5, as deprotonated functional groups (e.g., phenolic hydroxyl and carboxyl groups) enhance electron-donating capacity. Anoxic experiments and SOD quenching confirmed that direct electron transfer from phenolic groups was negligible, and $O_2^{\cdot-}$ was the exclusive key intermediate for Ag^+ reduction. Nano400 exhibits superior reduction activity compared to nano700, attributed to its higher abundance of oxygen-containing functional groups (e.g., phenolic hydroxyl groups up to 3.01 mmol g^{-1}), stronger electron-donating capacity, and greater production of $O_2^{\cdot-}$—the key intermediate mediating Ag^+ reduction to AgNPs, as confirmed by quenching experiments, EPR analysis, and cyclic voltammetry. Additionally, there is an optimal dosage range for nano-BC ($\leq$10 mg L^{-1} for nano400 and $\leq$20 mg L^{-1} for nano700). Excessive dosage may lead to excessive adsorption of Ag^+, intensified aggregation of nano-BC, and increased self-consumption of ROS, thereby inhibiting AgNPs formation. The synthesized AgNPs are quasi-spherical with a face-centered cubic structure, as characterized by HRTEM, EDS, and SAED. Overall, this research elucidates the structure–activity relationship between nano-BC properties and Ag^+ reduction efficiency, identifies the core role of pH and $O_2^{\cdot-}$ in the reaction, and provides valuable theoretical support and practical guidance for the design of efficient nano-BC-based materials for the remediation of Ag^+-contaminated water, with potential implications for environmental pollution control and catalytic applications. It should be noted that all experiments herein were performed in ultrapure water systems. Moreover, further multi-cycle recycling and long-term stability assessments of nano-BC will be conducted to evaluate its reusability for real water remediation. Converting toxic Ag^+ into nano-BC-reduced AgNPs largely mitigates aquatic ecological risks, although detached AgNPs under complex water conditions still pose latent threats to aquatic biota, and further ecotoxicity tests will be carried out to evaluate the corresponding biosafety. Practical silver wastewater contains variable dissolved oxygen, high ionic strength and competing ions that interfere with Ag^+ reduction by nano-BC, which we will quantify in future work.

Supplementary Information

The online version contains supplementary material available at https://doi.org/10.1007/s42773-026-00651-7.

Supplementary Material 1.

Acknowledgements
We greatly appreciate the valuable comments and suggestions from editors and anonymous reviewers.

Author contributions
Shiguo Gu: Writing—original draft, Writing—review & editing, Funding acquisition, Data curation. Dandan Wang: Writing—review & editing, Methodology, Formal analysis. Tongtong Wang: Writing—review & editing, Methodology. Wei Zhu: Writing—review & editing, Supervision, Investigation. All authors read and approved the final manuscript.

Funding
The authors gratefully acknowledge the Key Research Project of Natural Science in Colleges and Universities of Anhui Province (2025AHGXZK30307), Funding Project for Young Backbone Teachers to Visit and Study in China (JNFX2023061), Chuzhou University Research Initiation Fund Project (2023qd49, 2023qd44).

Data availability
Data will be made available on request.

Declarations

Competing interests
The authors declare that they have no known competing financial interests or personal relationships that could have appeared to influence the work reported in this paper.

Author details
[1]College of Civil and Architecture Engineering, Chuzhou University, Chuzhou 239000, China. [2]Institute for Interdisciplinary and Innovation Research, Xi'an University of Architecture and Technology, Xi'an 710055, China.

Received: 10 February 2026 Revised: 3 July 2026 Accepted: 19 July 2026
Published online: 26 August 2026

References

Adegboyega NF, Sharma VK, Siskova K, Zbořil R, Sohn M, Schultz BJ, Banerjee S (2012) Interactions of aqueous Ag^+ with fulvic acids: mechanisms of silver nanoparticle formation and investigation of stability. Environ Sci Technol 47(2):757–764

Bardestani R, Kaliaguine S (2018) Steam activation and mild air oxidation of vacuum pyrolysis biochar. Biomass Bioenergy 108:101–112

Cao X, Ma C, Zhao J, Guo H, Dai Y, Wang Z, Xing B (2019) Graphene oxide mediated reduction of silver ions to silver nanoparticles under environmentally relevant conditions: kinetics and mechanisms. Sci Total Environ 679:270–278

Chen X, Alvarez PJ, Masiello CA (2025) Environmentally persistent free radicals in biochar: environmental context and future research needs. Environ Sci Technol 59(23):11440–11454

Cymes BA, Krekeler MP, Nicholson KN, Grigsby JD (2017) A transmission electron microscopy (TEM) study of silver nanoparticles associated with mine waste from new Caledonian nickel deposits: potential origins of silver toxicity in a world heritage site. Environ Earth Sci 76:640

Dang F, Wang Q, Cai W, Zhou D, Xing B (2020) Uptake kinetics of silver nanoparticles by plant: relative importance of particles and dissolved ions. Nanotoxicology 14:654–666

Dong X, Ma LQ, Zhu Y, Li Y, Gu B (2013) Mechanistic investigation of mercury sorption by Brazilian pepper biochars of different pyrolytic temperatures based on X-ray photoelectron spectroscopy and flow calorimetry. Environ Sci Technol 47:12156–12164

Fu H, Zhou Z, Zheng S, Xu Z, Alvarez PJ, Yin D, Qu X, Zhu D (2018) Dissolved mineral ash generated by vegetation fire is photoactive under the solar spectrum. Environ Sci Technol 52:10453–10461

Gao X, Wu H (2014) Aerodynamic properties of biochar particles: effect of grinding and implications. Environ Sci Technol Lett 1(1):60–64

Gao B, Zhu S, Gu J, Liu Y, Yi X, Zhou H (2022) Superoxide radical mediated Mn(III) formation is the key process in the activation of peroxymonosulfate (PMS) by Mn-incorporated bacterial-derived biochar. J Hazard Mater 431:128549

Ge C, Huang D, Wang D, Zhang E, Li M, Zhu F, Zhu C, Chen N, Wu S, Zhou D (2022) Biotic process dominated the uptake and transformation of Ag^+ by *Shewanella oneidensis* MR-1. Environ Sci Technol 56:2366–2377

Gu S, Lian F, Han Y, Taherymoosavi S, Mitchell D, Joseph S, Wang Z, Xing B (2022) Nano-biochar modulates the formation of iron plaque through facilitating iron-involved redox reactions on aquatic plant root surfaces. Environ Sci Nano 9:1974–1985

Gu S, Sun B, Wang F, Zhu W, Lian F, Li J (2025) Insight into the crucial role of nano-biochar in the natural formation and bioaccumulation of silver nanoparticles in the rhizosphere by single-particle ICP-MS. Biochar 7:111

Hanna AL, Hamouda HM, Goda HA, Sadik MW, Moghanm FS, Ghoneim AM, Alenezi MA, Alnomasy SF, Alam P (2022) Elsayed TR (2022) Biosynthesis and characterization of silver nanoparticles produced by Phormidium ambiguum and Desertifilum tharense cyanobacteria. Bioinorg Chem Appl 1:9072508

Hou WC, Stuart B, Howes R, Zepp RG (2013) Sunlight-driven reduction of silver ions by natural organic matter: formation and transformation of silver nanoparticles. Environ Sci Technol 47:7713–7721

Huang YN, Qian TT, Dang F, Yin YG, Li M, Zhou DM (2019) Significant contribution of metastable particulate organic matter to natural formation of silver nanoparticles in soils. Nat Commun 10:3775

Jiang Y, Liu D, Cho M, Lee SS, Zhang F, Biswas P, Fortner JD (2016) In situ photocatalytic synthesis of Ag nanoparticles (nAg) by crumpled graphene oxide composite membranes for filtration and disinfection applications. Environ Sci Technol 50:2514–2521

Jones AM, Garg S, He D, Pham AN, Waite TD (2011) Superoxide-mediated formation and charging of silver nanoparticles. Environ Sci Technol 45:1428–1434

Kaliappan K, Nagarajan P, Jayabalan J, Pushparaj H, Elumalai S, Paramanathan B, Manickam V, Jang HT, Mani G (2025) Systematic antimicrobial, biofilm, free radical inhibition and tyrosinase inhibition assessments of efficient green silver nanoparticles from the aqueous root extract of *Cyphostemma adenocaule* (CA). RSC Pharm 2(1):147–162

Klupfel L, Keiluweit M, Kleber M, Sander M (2014) Redox properties of plant biomass-derived black carbon (biochar). Environ Sci Technol 48:5601–5611

Li L, Wang X, Fu H, Qu X, Chen J, Tao S, Zhu D (2020) Dissolved black carbon facilitates photoreduction of Hg(II) to Hg(0) and reduces mercury uptake by lettuce (*Lactuca sativa* L.). Environ Sci Technol 54:11137–11145

Lian F, Xing B (2024) From bulk to nano: formation, features, and functions of nano-black carbon in biogeochemical processes. Environ Sci Technol 58(36):15910–15925

Lian F, Yu W, Wang Z, Xing B (2018) New insights into black carbon nanoparticle-induced dispersibility of goethite colloids and configuration-dependent sorption for phenanthrene. Environ Sci Technol 53(2):661–670

Lian F, Yu W, Zhou Q, Gu S, Wang Z, Xing B (2020) Size matters: nano-biochar triggers decomposition and transformation inhibition of antibiotic resistance genes in aqueous environments. Environ Sci Technol 254(14):8821–8829

Lian F, Zhang Y, Gu S, Han Y, Cao X, Wang Z, Xing B (2021) Photochemical transformation and catalytic activity of dissolved black nitrogen released from environmental black carbon. Environ Sci Technol 55(9):6476–6484

Liu G, Zheng H, Jiang Z, Zhao J, Wang Z, Pan B, Xing B (2018) Formation and physicochemical characteristics of nano biochar: insight into chemical and colloidal stability. Environ Sci Technol 52(18):10369–10379

Liu Z, Ha S, Liu Y, Wang F, Tao F, Xu B, Yu R, Wang G, Ren F, Li H (2023) Application of Ag-based materials in high-performance lithium metal anode: a review. J Mater Sci Technol 133:165–182

Mahmoud SE, Ursueguia D, Mahmoud ME, Abdel-Fattah TM, Díaz E (2024) Functional surface homogenization of nanobiochar with cation exchanger for improved removal performance of methylene blue and lead pollutants. Biomass Convers Biorefin 14(16):19107–19127

Mekonnen B, Wilske B, Addisu B, Nigussie A, Siegfried K, Gizachew S, Yimer T, Mohammed B, Ahmed M, Abera T, Nebiyu A, Worku R, Regassa A, Firomsa T, Husien A, Worku G, Lema A, Tilahun A, Assefa K, Dume B, Eshete G, Pollex A (2025) Biochar-based fertilizers increase crop yields in acidic tropical soils. Biofuels Bioprod Biorefin 19:1124–1142

Nguyen TT, Zhang P, Bi J, Nguyen NH, Dang Y, Xu Z, Wang H, Ninan N, Bright R, Pham T, Nguyen CK, Sabri Y, Nguyen MT, Vongsvivut J, Zhao Y, Vasilev K, Truong VK (2024) Silver—gallium nano-amalgamated particles as a novel, biocompatible solution for antibacterial coatings. Adv Funct Mater 34(31):2310539

Peng H, Guo H, Gao P, Zhou Y, Pan B, Xing B (2021) Reduction of silver ions to silver nanoparticles by biomass and biochar: mechanisms and critical factors. Sci Total Environ 779:146326

Posachayanan N, Liwetpitaya P, Thoumrungroj A, Longchin P, Saengpitak K, Tuntithavornwat S, Kannan AM, Hunsom M (2024) Highly-efficient

recovery of silver from industrial cyanide-based plating effluent on TiO_2/activated carbon composites. Chemosphere 367:143614
Rashid MS, Liu G, Yousaf B, Hamid Y, Rehman A, Arif M, Ahmed R, Ashraf A, Song Y (2022) A critical review on biochar-assisted free radicals mediated redox reactions influencing transformation of potentially toxic metals: occurrence, formation, and environmental applications. Environ Pollut 315:120335
Ruan X, Sun Y, Du W, Tang Y, Liu Q, Zhang Z, Doherty W, Frost RL, Qian G, Tsang DC (2019) Formation, characteristics, and applications of environmentally persistent free radicals in biochars: a review. Bioresour Technol 281:457–468
Shahzadi S, Fatima S, Shafiq Z, Janjua MR (2025) A review on green synthesis of silver nanoparticles (SNPs) using plant extracts: a multifaceted approach in photocatalysis, environmental remediation, and biomedicine. RSC Adv 15(5):3858–3903
Shao P, Chang Z, Li M, Lu X, Jiang W, Zhang K, Luo X, Yang L (2023) Mixed-valence molybdenum oxide as a recyclable sorbent for silver removal and recovery from wastewater. Nat Commun 14:1365
Shapkin ND, Kopytov GF, Hernandez-Caceres JL, Filippov MV, Yakovenko NA, Moiseev AV, Dzhimak SS (2026) Review of silver nanoparticle synthesis methods in comparison with a hybrid photochemical reduction method. Russ Phys J 1–13
Sun X, Luo X, Zhang X, Xie J, Jin S, Wang H, Zheng X, Wu X, Xie Y (2019) Enhanced superoxide generation on defective surfaces for selective photooxidation. J Am Chem Soc 141:3797–3801
Sun Y, Zong T, Wu Q, Wang X, Hou H, Xin X, Xie J, Zhou Y, Yang J (2025) Fabrication of rice straw nano-biochar by ball milling for efficient adsorption of ammonium nitrogen and reduction of ammonia volatilization: effects and mechanisms. Environ Sci Nano 12(6):3122–3138
Tomczyk A, Sokołowska Z, Boguta P (2020) Biomass type effect on biochar surface characteristic and adsorption capacity relative to silver and copper. Fuel 278:118168
Uchimiya M, Lima IM, Thomas Klasson K, Chang S, Wartelle LH, Rodgers JE (2010) Immobilization of heavy metal ions (Cu^{II}, Cd^{II}, Ni^{II}, and Pb^{II}) by broiler litter-derived biochars in water and soil. J Agric Food Chem 58(9):5538–5544
Vrček IV, Žuntar I, Petlevski R, Pavičić I, Dutour Sikirić M, Ćurlin M, Goessler W (2016) Comparison of in vitro toxicity of silver ions and silver nanoparticles on human hepatoma cells. Environ Toxicol 31:679–692
Wang D, Zhang W, Hao X, Zhou D (2013) Transport of biochar particles in saturated granular media: effects of pyrolysis temperature and particle size. Environ Sci Technol 47(2):821–828
Wang Y, Lin Q, Liu Z, Liu K, Wang X, Shang J (2023) Salt-affected marginal lands: a solution for biochar production. Biochar 5:21
Xin D, Xian M, Chiu PC (2019) New methods for assessing electron storage capacity and redox reversibility of biochar. Chemosphere 215:827–834
Xu Z, Xu X, Tao X, Yao C, Tsang DC, Cao X (2019) Interaction with low molecular weight organic acids affects the electron shuttling of biochar for Cr(VI) reduction. J Hazard Mater 378:120705
Yang P, Peng J, Chu Z, Jiang D, Jin W (2017) Facile synthesis of Prussian blue nanocubes/silver nanowires network as a water-based ink for the direct screen-printed flexible biosensor chips. Biosens Bioelectron 92:709–717
Zhang X, Yang CW, Yu HQ, Sheng GP (2016) Light-induced reduction of silver ions to silver nanoparticles in aquatic environments by microbial extracellular polymeric substances (EPS). Water Res 106:242–248
Zhang X, Sun P, Wei K, Huang X, Zhang X (2020) Enhanced H_2O_2 activation and sulfamethoxazole degradation by Fe-impregnated biochar. Chem Eng J 385:123921
Zhang R, Li X, Lv Z, Qi W, Wu W, Chen X, Li Z (2026) Interlayer-confined redox assembly creates a continuous, addressable phase for coupled mass-energy transport in lamellar membranes. Nano Lett 26:7738–7748
Zhao X, Zhou L, Xu X, Ai C, Zhao P, Yan L, Jiang C, Shi J (2021) Recovery of Ag^+ by cyclic lipopeptide iturin A and corresponding chain peptide: reaction mechanisms, kinetics, toxicity reduction, and applications. Sci Total Environ 763:142988
Zhong D, Jiang Y, Zhao Z, Wang L, Chen J, Ren S, Liu Z, Zhang Y, Tsang DC, Crittenden JC (2019) pH dependence of arsenic oxidation by rice-husk-derived biochar: roles of redox-active moieties. Environ Sci Technol 53:9034–9044
Zhu Y, Wei J, Li J (2023) Decontamination of Cr (VI) from water using sewage sludge-derived biochar: role of environmentally persistent free radicals. Chin J Chem Eng 56:97–103
Zhu K, Ma S, Chen N, Dai Y, Wang T, Guo X, Jia H (2024) Robust reactive oxygen species production in interfacial reaction between organic acids and biochar: the combined effect of electron acceptance and electron conduction. J Hazard Mater 464:132960
Zollo A, Gottuso A, Palmisano L, Giamello E, Parrino F, Livraghi S (2025) Reaction of nitrate radicals and DMPO in non-aqueous media: a novel detection tool to highlight the nitrate radical role in photocatalytic processes. Angew Chem Int Ed Engl 64(23):e202505313